International Journal of Minerals, Metallurgy and Materials
Volume 21, Number 5, May 2014, Page 438
DOI: 10.1007/s12613-014-0927-4

Precipitation behavior and martensite lath coarsening during tempering of T/P92 ferritic heat-resistant steel

Lin-qing Xu[1)], *Dan-tian Zhang*[1)], *Yong-chang Liu*[1)], *Bao-qun Ning*[1,2)], *Zhi-xia Qiao*[1,3)], *Ze-sheng Yan*[1)], *and Hui-jun Li*[1)]

1) State Key Lab of Hydaulic Engineering Simulation and Safety, School of Material Science and Engineering, Tianjin University, Tianjin 300072, China
2) School of Materials Science and Engineering, Tianjin University of Technology, Tianjin 300384, China
3) School of Mechanical Engineering, Tianjin University of Commerce, Tianjin 300134, China
(Received: 26 November 2013; revised: 10 January 2014; accepted: 16 January 2014)

Abstract: Tempering is an important process for T/P92 ferritic heat-resistant steel from the viewpoint of microstructure control, as it facilitates the formation of final tempered martensite under serving conditions. In this study, we have gained deeper insights on the mechanism underlying the microstructural evolution during tempering treatment, including the precipitation of carbides and the coarsening of martensite laths, as systematically analyzed by optical microscopy, transmission electron microscopy, and high-resolution transmission electron microscopy. The chemical composition of the precipitates was analyzed using energy dispersive X-ray spectroscopy. Results indicate the formation of M_3C (cementite) precipitates under normalized conditions. However, they tend to dissolve within a short time of tempering, owing to their low thermal stability. This phenomenon was substantiated by X-ray diffraction analysis. Besides, we could observe the precipitation of fine carbonitrides (MX) along the dislocations. The mechanism of carbon diffusion controlled growth of $M_{23}C_6$ can be expressed by the Zener's equation. The movement of Y-junctions was determined to be the fundamental mechanism underlying the martensite lath coarsening process. Vickers hardness was estimated to determine their mechanical properties. Based on the comprehensive analysis of both the microstructural evolution and hardness variation, the process of tempering can be separated into three steps.

Keywords: ferritic steel; heat resisting; tempering; precipitation; martensite; coarsening

1. Introduction

Ferritic heat-resistant 9wt%–12wt% Cr steels have been widely used in power plants operated under supercritical or ultra-supercritical conditions owing to their ability to withstand high temperatures, good creep resistance properties, excellent heat conductivity, low thermal expansion coefficient, and high performance-cost ratio [1–2]. Recently, Cr–W steels have attracted great attention as a potential alternative to conventional Cr–Mo (P91) steels, from the viewpoint of reduced radioactivation of fusion components. Furthermore, Cr–W steels are considered to be promising structural materials owing to their excellent high-temperature performance compared with traditional Cr–Mo steels. Besides, modification of T/P91 steel (modified 9Cr–1Mo steel) by the addition of 1.8wt% W and the reduction of Mo content from 1wt% to 0.5wt% results in the formation of T/P92 steel with enhanced stress rupture strength [3–4].

Tempering treatment is an important process in T/P92 steel to obtain suitable microstructure and mechanical performance [5–6]. Thus far, several studies have analyzed the tempering behavior of T/P92 [7–10], particularly, during long-term tempering treatment. Nevertheless, very few reports have analyzed the early stages of the tempering process. According to the study reported by Caron, the martensitic sub-structure of Fe–0.2C steel is more defined upon rapid tempering at 690°C for 0.28 s; besides, carbides tend to precipitate, despite the extremely short tempering time [11]. These results suggest that the tempering process might take place even within a very short time. As the T/P92 steel is a more complex system with a lower carbon content

Corresponding author: Yong-chang Liu E-mail: licmtju@163.com

compared with Fe–0.2C steel, tempering behavior during the early stages in the former is expected to be different from that in the latter. To this end, this work aims to study the structure evolution in T/P92 steel during the early stage of the tempering process, including the precipitation behavior and martensite lath coarsening.

2. Experimental procedures

The experimental material was supplied by Tianjin Pipe Corporation, and its chemical composition is provided in Table 1. The raw material was first hot rolled at 950°C to form a pipe, followed by air-cooling to room temperature. To increase the heating and cooling rates, the samples were cut into small sheets with the dimension 10 mm × 10 mm × 0.3 mm. The heat treatment performed in this study is as follows. Firstly, the sheets were austenitized at 1050°C for 1800 s in a vacuum furnace, followed by air-cooling (normalizing) to room temperature. Subsequently, the samples were tempered at 650°C for various durations from 10 to 3.6 × 10^5 s.

Table 1. Chemical composition of the experimental T/P92 steel wt%

W	C	Si	Mn	Ni	Cr	Mo	Cu	Al	V	B	Nb
1.77	0.09	0.42	0.40	0.20	8.95	0.33	0.03	0.016	0.18	0.0013	0.06

The microstructure of the samples was observed by optical microscopy (OM) and transmission electron microscopy (TEM) (JEM-2100F). Thin foils for TEM observation were prepared as the following. Firstly, the sample sheets were mechanically polished to a thickness of 50 μm using emery paper, followed by double-jet electrolytic polishing using the solution of 5vol% perchloric acid-ethyl alcohol. The average width of the martensite laths and the average diameter of the precipitates were estimated from TEM images. The chemical composition of the precipitates was analyzed using energy dispersive X-ray spectroscopy (EDS). The chemical extraction was conducted in the solution containing 15vol% HCl, wherein the matrix was dissolved under this condition, leaving behind the precipitates [12]. Furthermore, the composition of the chemical extraction was analyzed by X-ray diffraction (XRD) (Rigaku D/max 2500 v/pc with Cu source). The Vickers hardness (ISO 6507-1:2005 Ed. 3) was tested by applying a load of 0.49 N after mechanical polishing.

3. Experimental results

3.1. Microstructure after the normalization process

The microstructure of T/P92 samples was observed by OM and TEM, after normalizing at 1050°C for 1800 s. The OM image of the sample shown in Fig. 1(a) indicates that the microstructure after the normalization process is all martensite which distributed within the parent austenite grains. The martensite has an elongated lath structure with a high density of dislocations. The lath structure is composed of packets, which are group of laths with almost the same plane. The white dotted lines shown in Fig. 1(b) represent the boundaries of packets, wherein small martensite laths are distributed. The average width of the martensitic laths is approximately (0.2 ± 0.02) μm.

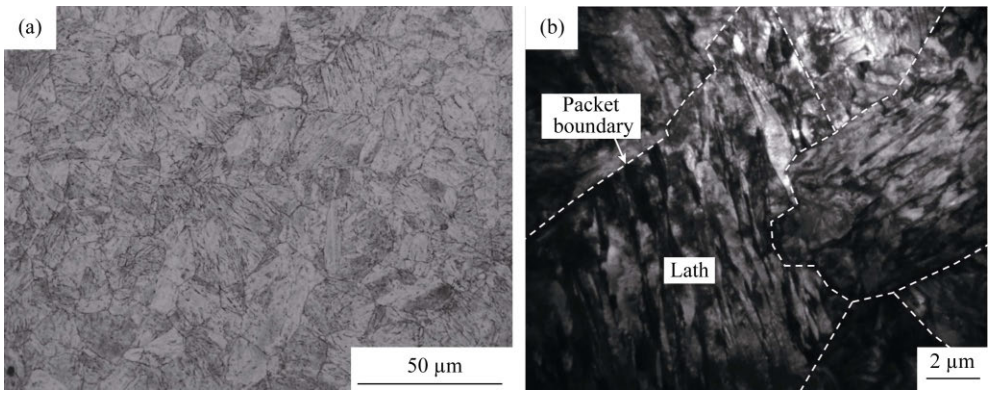

Fig. 1. Microstructures of T/P92 steel normalized at 1050°C for 1800 s: (a) OM image; (b) TEM image.

After the normalizing process, needle-like precipitates were observed in the matrix, which were identified as M_3C precipitates. The precipitation of M_3C is reported to be typical of the normalization process [13–14]. Fig. 2 shows the bright and dark field images of the region containing M_3C precipitates. The corresponding selected area electron diffraction (SAED) pattern is shown in Fig. 2(b). It shows that the nucleation of M_3C is mainly homogeneous and does not seem to depend on crystal defects, such as dislocations and grain boundaries [15].

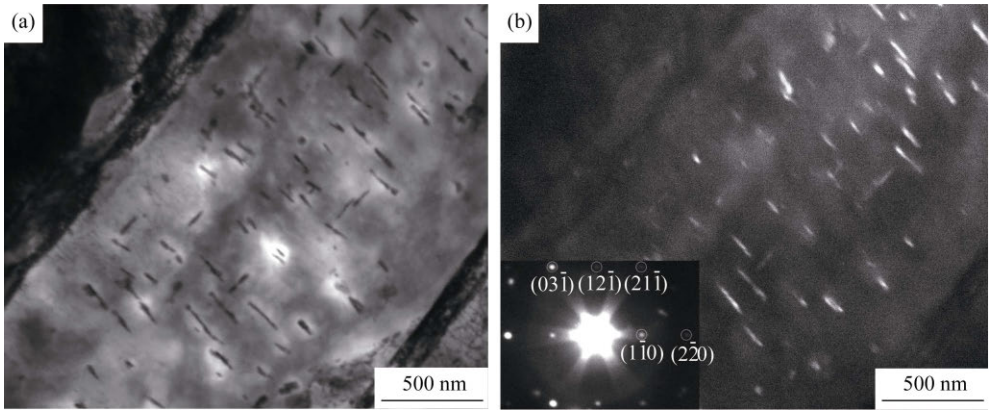

Fig. 2. TEM images of M_3C precipitates in the sample after normalizing: (a) bright field image; (b) dark field image.

Fig. 3 shows the high-resolution transmission electron microscopy (HRTEM) image of a single needle-like M_3C particle. The corresponding enlarged view of the particle clearly shows the lattices. Fig. 4(a) shows the fast Fourier transformation (FFT) of the image, showing the crystallographic indices and zone axis of M_3C. Fig. 4(b) shows the SAED pattern of the matrix around this M_3C precipitate, indicating the [111] zone axis of the matrix. Using this, we determined the relationship of $[113]_{M_3C}//[111]_{\alpha-Fe}$. The chemical composition of M_3C precipitates was analyzed using energy dispersive X-ray spectroscopy (EDS), as shown in Fig. 5, here M is Fe. In the figure, the additional elements Cr and W are from the matrix.

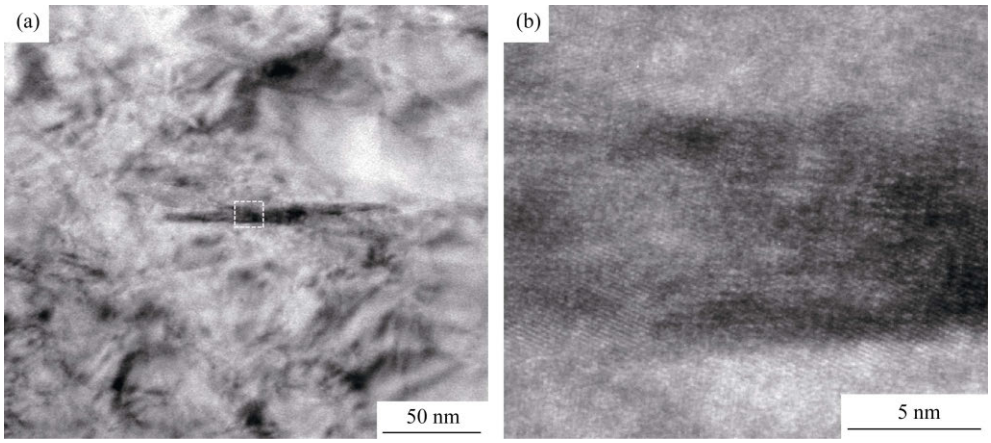

Fig. 3. HRTEM images of a single M_3C particle: (a) morphology of a single M_3C particle; (b) enlarged image of the region shown in (a).

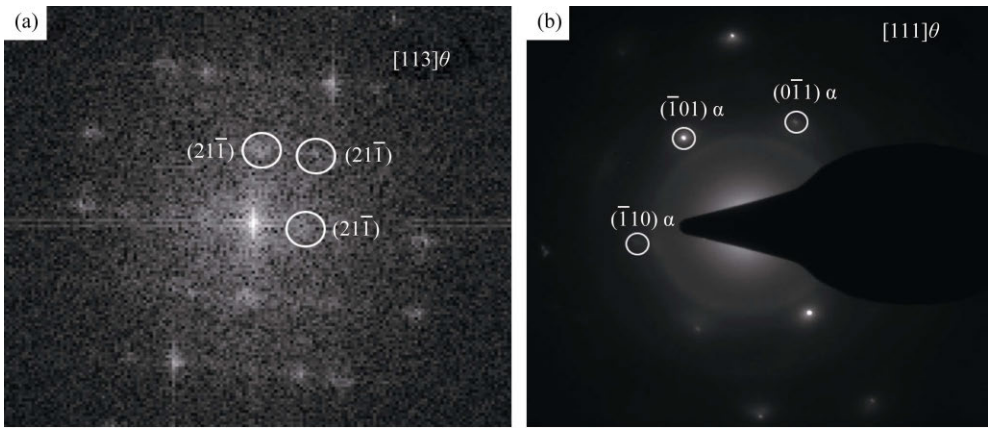

Fig. 4. Crystal face index and zone axis of M_3C and the surrounding matrix: (a) FFT image of M_3C; (b) SAED pattern of the surrounding matrix.

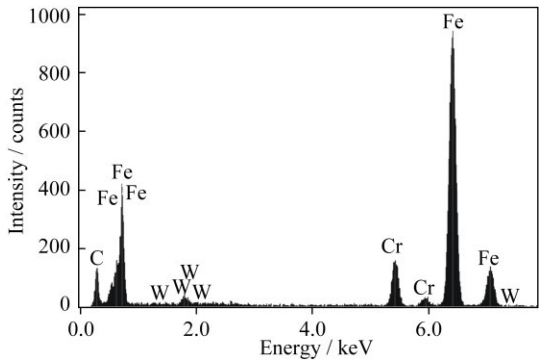

Fig. 5. EDS spectrum of the area around the M_3C precipitate.

3.2. Microstructural evolution during tempering

The microstructural evolution during tempering consists of two parts, namely, the precipitation and growth of carbides, and the coarsening of martensite lath [11]. After the normalization process, the martensite structure is supersaturated at room temperature [16]. Therefore, when tempered at high temperature, the carbides precipitate within the lath or along the boundaries of laths and parent austenite grains. The microstructural evolution during tempering can be clearly observed by OM, as shown in Fig. 6. After tempering for 120 s, the boundaries of laths and parent austenite become clear, as shown in Fig. 6(a). Increasing the tempering time to 3600 (Fig. 6(b)) and 7200 s (Fig. 6(c)), carbides precipitate significantly along the boundaries or within the grains. Further prolonging the tempering treatment time to 3.6×10^5 s results in the precipitation of a large amount of carbides, leading to the coarsening of grain boundaries (Fig. 6(d)).

The microstructural evolution in tempered samples was further observed using TEM (Fig. 7). In case of the sample tempered for only 10 s, $M_{23}C_6$ carbides are precipitated along the lath boundaries and parent austenite grain boundaries, as shown in Fig. 7(a). This suggests that the $M_{23}C_6$ precipitation takes place immediately at the beginning of tempering treatment. In the samples tempered at 650°C for 10 and 120 s (as shown in Fig. 7(b)), needle-like M_3C carbides are formed in addition to $M_{23}C_6$, as shown by arrows. When tempered for 3600 s, there is a significant increase in the width of the laths and the size of $M_{23}C_6$, in addition to the disappearance of M_3C, as shown in Fig. 7(c). Tempering for up to 3.6×10^5 s (Fig. 7(d)) results in the formation of equiaxed grains with low dislocation density, owing to the recovery and recrystallization of martensite. Besides, the sample tempered for 3.6×10^5 s shows fine carbonitrides (MX) along the dislocations, where it is easy for MX to precipitate because of low nucleation activation energy (shown by the arrows in Fig. 7(d)). These dispersed fine MX can provide significant pinning effect to obstruct the dislocation gliding, thereby resulting in the strengthening of performance [17].

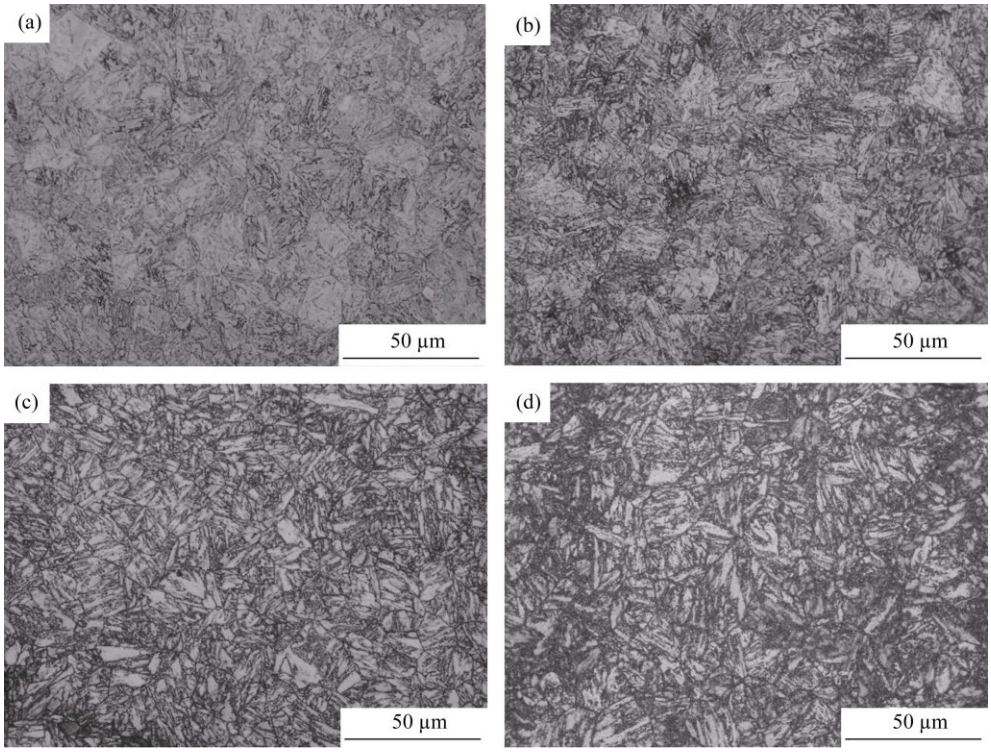

Fig. 6. OM images of T/P92 steel tempered at 650°C for different time: (a) 120 s; (b) 3600 s; (c) 7200 s; (d) 3.6×10^5 s.

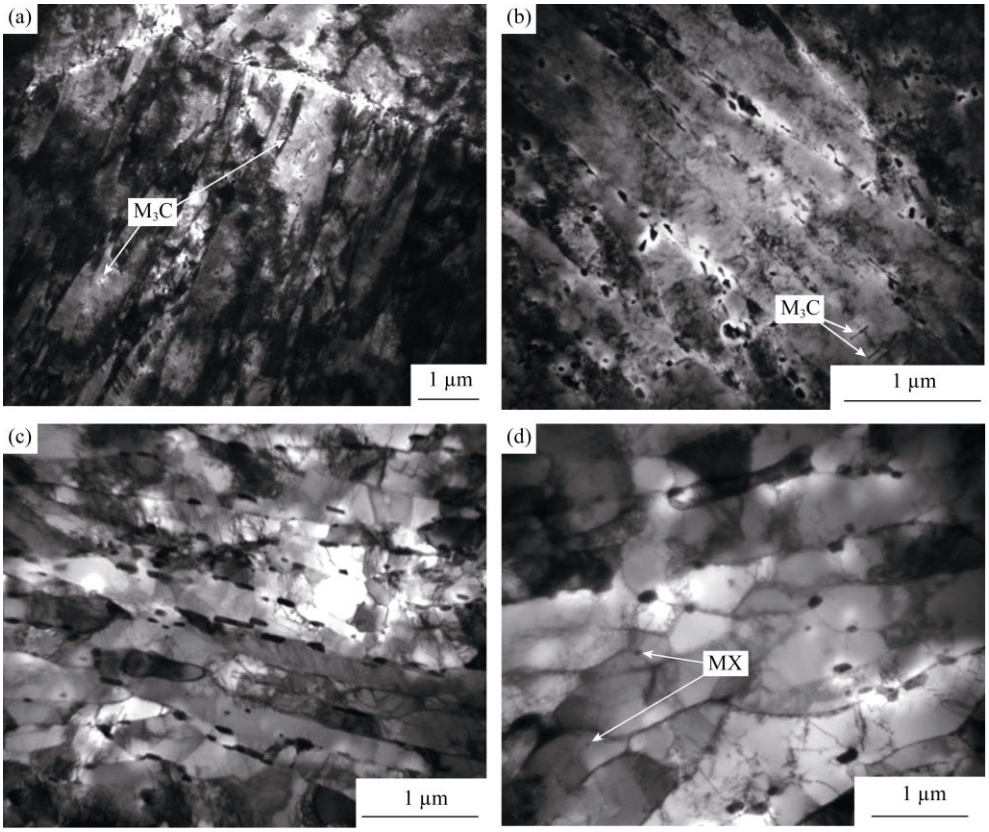

Fig. 7. TEM images of T/P92 steel tempered at 650°C for different time: (a) 10 s; (b) 120 s; (c) 3600 s; (d) 3.6×10^5 s.

Fig. 8 shows the HRTEM images of the $M_{23}C_6$ precipitate, clearly revealing the lattice pattern. Fig. 9 shows the FFT image of Fig. 8(b) and the SAED pattern of the matrix around this $M_{23}C_6$ precipitate. The result indicates the relationship of $[011]_{M_{23}C6}//[001]_{\alpha-Fe}$.

Fig. 10 shows the HRTEM images of MX with the size of approximately 50 nm. The FFT image of Fig. 10(b) and the SAED pattern of the matrix around this MX precipitate are shown in Fig. 11. From this, the relationship $[111]_{MX}//[113]_{\alpha-Fe}$ can be determined. Fig. 12 shows the chemical composition of $M_{23}C_6$ and MX, as determined from the EDS analysis. The results indicate that M in $M_{23}C_6$ is mainly Cr, and MX represent (Nb,V)(C,N). Note that, the additional elements Fe, W and Mo in Fig. 12(a), and Fe and Cr in Fig. 12(b) are from the matrix.

4. Discussion

4.1. Dissolution of M_3C

After normalization, M_3C precipitates have been found in

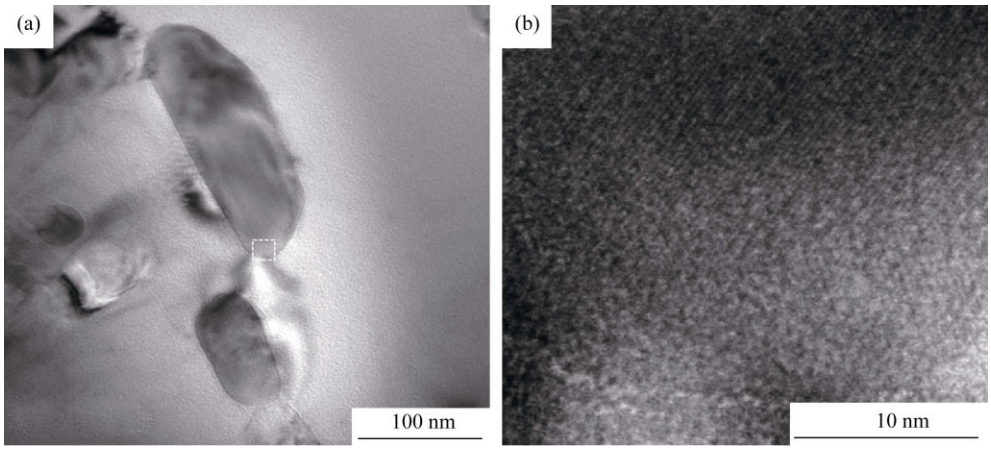

Fig. 8. HRTEM images of $M_{23}C_6$: (a) morphology of a single $M_{23}C_6$ particle; (b) enlarged image of the region shown in (a).

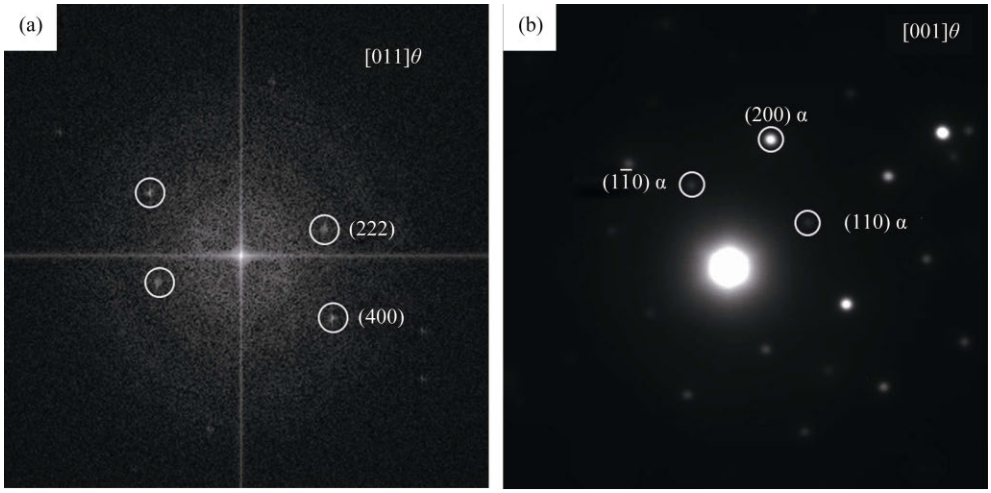

Fig. 9. Crystal face index and zone axis of $M_{23}C_6$ and the surrounding matrix: (a) FFT image of $M_{23}C_6$; (b) SAED pattern of the surrounding matrix.

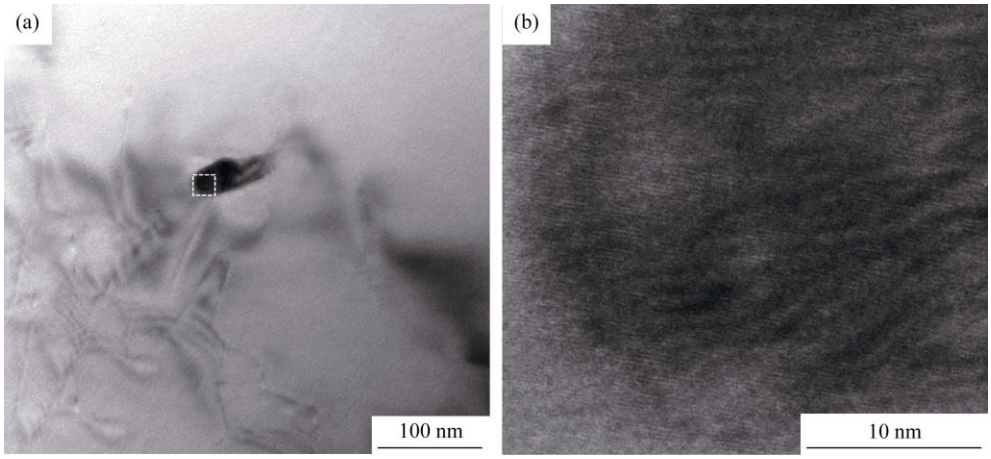

Fig. 10. HRTEM images of MX: (a) morphology of a single MX particle; (b) enlarged image of the region shown in (a).

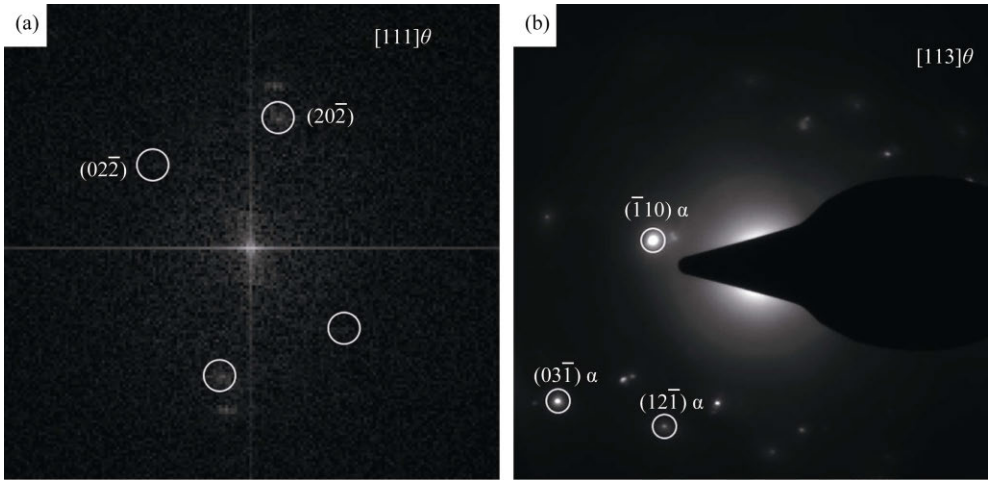

Fig. 11. Crystal face index and zone axis of MX and the surrounding matrix: (a) FFT image of MX; (b) SAED pattern of the surrounding matrix.

the matrix. However, M_3C precipitates can be typically dissolved within short tempering time because of their low thermal stability [18]. The composition of carbides during tempering was determined by performing the XRD analysis of the extracted chemical, as shown in Fig. 13. In case of the sample tempered at 650°C for 30 s, the main composition is

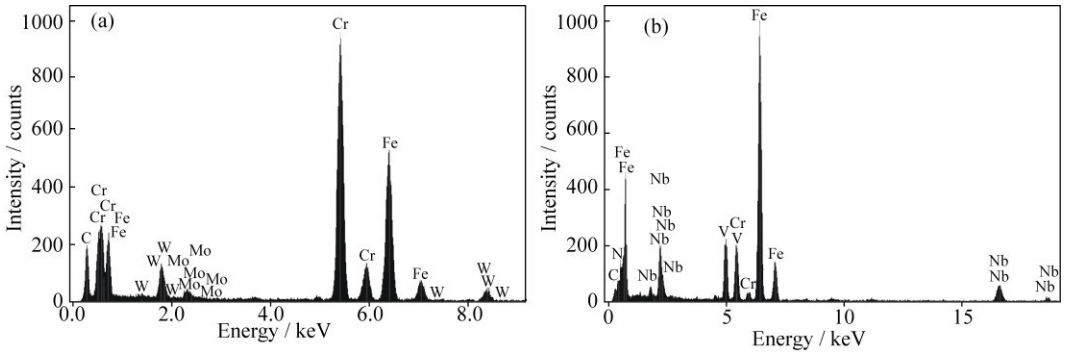

Fig. 12. EDS spectra of the regions around the $M_{23}C_6$ precipitate (a) and the MX precipitate (b).

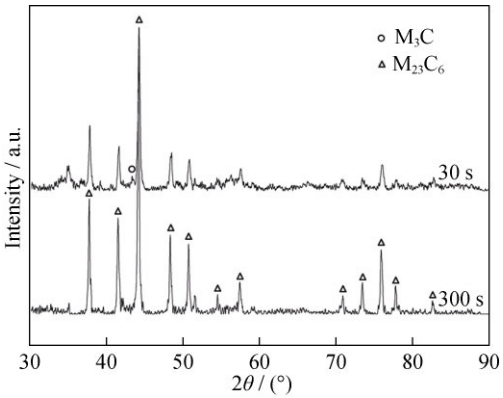

Fig. 13. XRD patterns of the chemical extracted from T/P92 steel after tempering at 650°C for different time: (a) 30 s; (b) 300 s.

$M_{23}C_6$. In addition, we could observe a small peak of M_3C at 2θ = 43.3°. Upon tempering at 650°C for 300 s, the peak corresponding to M_3C disappears, indicating that M_3C precipitates have been dissolved.

4.2. Precipitation of $M_{23}C_6$ during tempering

The nucleation of elongated $M_{23}C_6$ occurs along the lath and parent austenite grain boundaries. It is typically heterogeneous, with the critical nucleation size as small as several nanometers [19]. Once new nuclei are formed, these nucleation sites are no longer used for the formation of other nuclei. This leads to the rapid reduction of nucleation rate with time. On the other hand, for $M_{23}C_6$ precipitation, of which the phase transformation is determined by solute saturation, the solute concentration of the micro-region is reduced after the formation of new nuclei. This results in the rapid increase of critical nucleation energy, and thus a significant decrease in nucleation rate.

The $M_{23}C_6$ precipitate is a stable phase, which typically exists during long term tempering. Besides, $M_{23}C_6$ precipitates dispersed along the laths and grain boundaries endow T/P92 steel with good mechanical properties by blocking the movement of boundaries. However, the growth of $M_{23}C_6$ will take place during the high temperature tempering after nucleation. The 3-dimensional growth controlled by carbon diffusion can be described by the Zener equation [20]:

$$d = \alpha_3 (Dt)^{1/2} \tag{1}$$

where d is the average diameter at time t, D is the diffusion coefficient, and α_3 is a dimensionless time-independent growth coefficient. According to the hypothesis proposed by Zener, α_3 depends on the degree of supersaturation, which is a function of the concentration of solute elements in both $M_{23}C_6$ and the matrix [21]. Generally, diffusion coefficient D can be described by the Arrhenius equation:

$$D = D_0 \exp\left(\frac{-Q_d}{RT}\right) \tag{2}$$

where D_0 is the temperature-independent constant, Q_d is the diffusion activation energy.

For the diffusion of C in ferrite, $D_0 = 6.2\times10^{-7}$ m^2/s and $Q_d = 800$ kJ were obtained from previous work [22].

The measured average diameter of $M_{23}C_6$ and the fitted curve using Eq. (1) are shown in Fig. 14. The fitted curve and the experimental data are basically consistent, indicating that Eq. (1) is suitable for the description of $M_{23}C_6$ growth. The experimentally measured growth rate is rather slow, as shown in Fig. 14. This indicates that the precipitation of $M_{23}C_6$ is not only controlled by the diffusion of C but also the substantial elements, such as Cr, since the diffusion activation energy of Cr is much higher than that of C [23].

4.3. Coarsening of martensite laths during tempering

The recovery process, which includes the decrease of dislocation density and the evolution of morphology of lath structure, takes place markedly during tempering, as shown in Fig. 7. The evolution of lath structure morphology is caused by the movement of lath boundaries, which is driven by the strain accumulated from the martensitic transformation. Table 2 shows the change in the measured width of martensite laths after normalization and tempering treatment. It shows that the width of martensite laths increases con-

tinuously as a function of tempering time. Besides, it can be observed that the increase of lath width takes place significantly during the early stage of tempering treatment, but this tends to slow down, upon prolonging the tempering time. It indicates that a large amount of strain is generated during the martensitic transformation that provides large driving force for the movement of lath boundaries during the early stage of tempering treatment. The observed reduction in the increase rate of lath width with prolonged tempering time can be attributed to the following two factors: (1) the strain reduces gradually, thereby lowering the driving force for the movement of boundaries; (2) the movement of lath boundaries is obstructed by the pinning effect of precipitates.

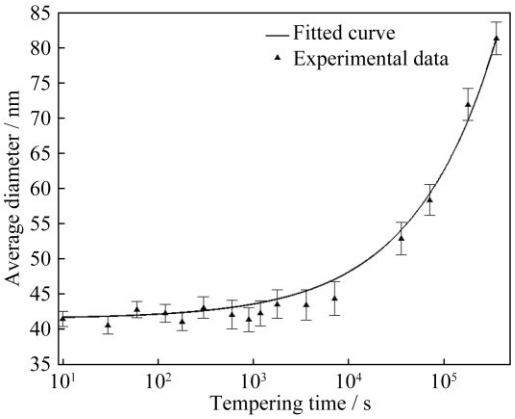

Fig. 14. Fitted curve and experimental data of the diameter of $M_{23}C_6$.

Table 2. Martensite lath width at different tempering time

Tempering time / s	Average lath width / μm
0	0.20
6×10^1	0.25
6×10^2	0.32
1.8×10^3	0.35
3.6×10^4	0.38
3.6×10^5	0.40

Previous studies have performed *in situ* analysis of the movement of lath boundaries [24]. The velocity of the movement of lath boundaries depends on their inherent characteristics, such as the misorientation and the difference of strain on both sides of each boundary. Since the strain does not distribute homogeneously in the lath structure, lath coarsening exhibits heterogeneity during the tempering treatment.

Moreover, the lath coarsening proceeds via the mechanisms associated with the movement of lath boundaries. Fig. 15 shows the TEM image of martensite laths after tempering at 650°C for 7200 s. Fig. 16 schematically illustrates the two mechanisms underlying the lath coarsening process. The TEM images indicate that some $M_{23}C_6$ particles distribute in a row in the matrix, as shown by an arrow in Fig. 15 (a). This row of $M_{23}C_6$ particles suggests a trace of lath boundary which, once present along the row, disappears after tempering. The disappearance of the lath could be attributed to the recovery of dislocations and the recombination of two adjacent lath boundaries caused by the movement. This is the first mechanism (process A) of lath coarsening shown in Fig. 16. However, there is no clear evidence to substantiate the presence of the row of carbides in this experiment as well as in previous work [25]. This implies that process A may not be the predominant mechanism of lath coarsening. On the other hand, the TEM image shown in Fig. 15(b) indicates the formation of some Y-junctions, which are formed via the interlacing of martensite laths. The movement of these Y-junctions (process B) is considered to be the fundamental process underlying the lath coarsening [25]. A great number of small angle Y-junctions that are formed during normalizing can be observed in Fig. 1(b), which are prepared for the lath coarsening during tempering. Upon prolonging the tempering time, we could observe the formation of equiaxed grains, which could be attributed to the movement of Y-junctions, as shown in Fig. 7(d). By then, strain relaxation leads to lowering of the moving velocity of lath boundaries, thereby slowing down the coarsening process.

4.4. Effects of microstructure on Vickers hardness

The Vickers hardness test was applied to characterize the effect of microstructure change on the mechanical properties after tempering. The change of Vickers hardness as a function of tempering time is shown in Fig. 17. This curve exhibits a constantly decrease with prolonging tempering time, and it consists basically of three steps according to the slope, as shown by dotted lines in the figure.

Accordingly, based on the comprehensive analysis of the abovementioned results and the value of Vickers hardness, the process of tempering can be separated into three steps. The tempering process during the initial 10 to 120 s is defined as the first step, where the Vickers hardness of the samples was found to decrease rapidly. This could be ascribed to the significant coarsening of martensite laths during the early stage of tempering. Here, the lath width is considered to be the critical factor determining the mechanical performance [26]. The tempering process from 120 to 3600 s is defined as the second step, during which the coarsening velocity of laths slows down as a result of low mobility of lath boundaries, leading to a slow decrease of Vickers hard-

ness. Finally, the process of tempering from 3600 to 3.6×10^5 s is defined as the third step, during which the carbides grow rapidly, together with the formation of equiaxed grains with low dislocation density. And the decrease of Vickers hardness is accelerated again because of the weak pinning effect associated with the significant growth of $M_{23}C_6$.

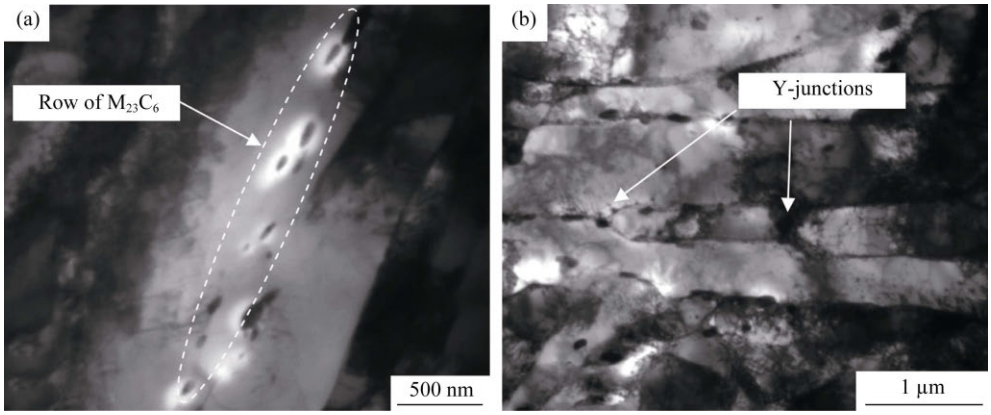

Fig. 15. TEM images of T/P92 steel tempered for 7200 s: (a) morphology of the $M_{23}C_6$ row; (b) morphology of Y-junctions.

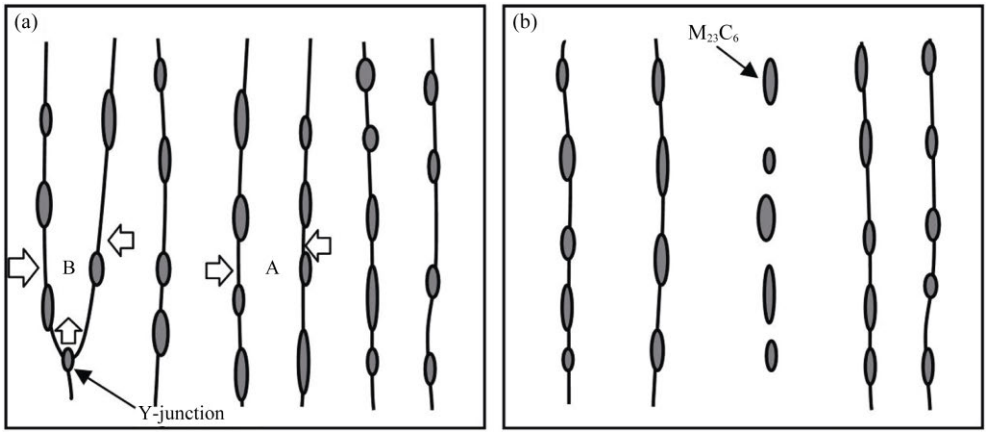

Fig. 16. Schematic diagram of the recovery process: (a) before recovery; (b) after recovery (process A shows the recombination of two boundaries, and process B shows the movement of Y-junctions).

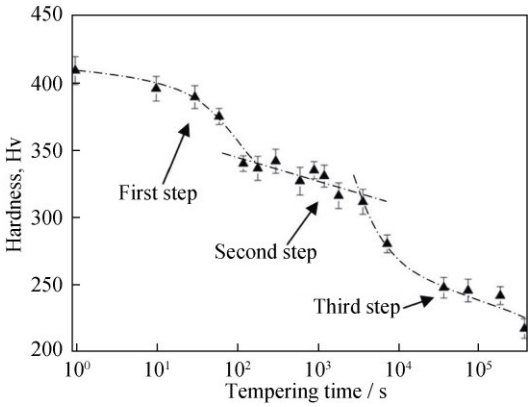

Fig. 17. Relationship of Vickers hardness and tempering time.

5. Conclusions

(1) Needle-like M_3C precipitated during air-cooling from the austenitizing temperature to room temperature is an unstable phase. This tends to disappear and will be replaced by the precipitation of stable $M_{23}C_6$. The tempering process, including the precipitation of carbides, coarsening of martensite laths, and dissolution of dislocation, takes place even within a very short time at 650°C.

(2) Fine MX carbonitrides are observed along dislocations within martensite laths. The growth of $M_{23}C_6$ can be described suitably by considering the carbon diffusion controlled 3-dimensional growth equation proposed by Zener. The fundamental mechanism underlying the lath coarsening process is the movement of Y-junctions, which occurs as a result of the strain generated from the martensitic transformation. Upon prolonging the tempering time, the rate of lath coarsening decreases because of the strain relaxation.

(3) The process of tempering can be separated into three steps according to the comprehensive analysis of microstructural evolution and the change of Vickers hardness.

Acknowledgements

This work was financially supported by the China National Funds for Distinguished Young Scientists (No. 51325401), the International Thermonuclear Experimental Reactor (ITER) Program Special Project (No. 2014GB125006), the National Natural Science Foundation of China (No. 51104107), and the Major State Basic Research Development Program (No. 2014CB046805).

References

[1] F. Abe, Precipitate design for creep strengthening of 9% Cr tempered martensitic steel for ultra-supercritical power plants, *Sci. Technol. Adv. Mater.*, 9(2008), art. No. 013002.

[2] B.Q. Ning, Q.Z. Shi, Z.S. Yan, J.C. Fu, Y.C. Liu, and L.J. Bie, Variation of martensite phase transformation mechanism in minor-stressed T91 ferritic steel, *J. Nucl. Mater.*, 393(2009), No. 1, p. 54.

[3] P.J. Ennis and A. Czyrska-Filemonowicz, Recent advances in creep-resistant steels for power plant applications, *Sadhana*, 28(2003), No. 3-4, p. 709.

[4] F. Abe, T. Horiuchi, M. Taneike, and K. Sawada, Stabilization of martensitic microstructure in advanced 9Cr steel during creep at high temperature, *Mater. Sci. Eng. A*, 378(2004), No. 1-2, p. 299.

[5] F. Liu, G. Xu, Y.L. Zhang, H.J. Hu, L.X. Zhou, and Z.L. Xue, *In situ* observations of austenite grain growth in Fe–C–Mn–Si super bainitic steel, *Int. J. Miner. Metall. Mater.*, 20(2013), No. 11, p. 1060.

[6] J.Y. Li, P. Zhao, J. Yanagioto, S. Sugiyama, and Y.L. Chen, Effects of heat treatment on the microstructures and mechanical properties of a new type of nitrogen-containing die steel, *Int. J. Miner. Metall. Mater.*, 19(2012), No. 6, p. 511.

[7] Z. Lu, R.G. Faulkner, N. Riddle, F.D. Martino, and K. Yang, Effect of heat treatment on microstructure and hardness of Eurofer 97, Eurofer ODS and T92 steels, *J. Nucl. Mater.*, 386-388(2009), p. 445.

[8] F. Abe, H. Araki, and T. Noda, The effect of tungsten on dislocation recovery and precipitation behavior of low-activation martensitic 9Cr steels, *Metall. Trans. A*, 22(1991), No. 10, p. 2225.

[9] F. Abe, Effect of quenching, tempering, and cold rolling on creep deformation behavior of a tempered martensitic 9Cr-1W steel, *Metall. Mater. Trans. A.*, 34(2003), No. 4, p. 913.

[10] H. Ghassemi-Armaki, R.P. Chen, K. Maruyama, M. Yoshizawa, and M. Igarashi, Static recovery of tempered lath martensite microstructures during long-term aging in 9–12% Cr heat resistant steels, *Mater. Lett.*, 63(2009), No. 28, p. 2423.

[11] G.R. Speich and W.C. Leslie, Tempering of steel, *Mater. Trans.*, 3(1972), No. 5, p. 1043.

[12] H. Sakasegawa, M. Tamura, S. Ohtsuka, S. Ukai, H. Tanigawa, A. Kohyama, and M. Fujiwara, Precipitation behavior of oxide particles in mechanically alloyed powder of oxide-dispersion-strengthened steel, *J. Alloys Compd.*, 452(2008), No. 1, p. 2.

[13] C.X. Liu, D.T. Zhang, Y.C. Liu, Q. Wang, and Z.S. Yan, Investigation on the precipitation behavior of M_3C phase in T91 ferritic steels, *Nucl. Eng. Des.*, 241(2011), p. 2411.

[14] B. Hutchinson, J. Hagström, O. Karlsson, D. Lindell, M. Tornberg, F. Lindberg, and M. Thuvander, Microstructures and hardness of as-quenched martensites (0.1–0.5%C), *Acta Mater.*, 59(2011), No. 14, p. 5845.

[15] G. Ghosh and G.B. Olson, Precipitation of paraequilibrium cementite: Experiments, and thermodynamic and kinetic modeling, *Acta Mater.*, 50(2002), No. 8, p. 2099.

[16] Å. Gustafson and M. Hättestrand, Coarsening of precipitates in an advanced creep resistant 9% chromium steel quantitative microscopy and simulations, *Materi. Sci. Eng. A.*, 333(2002), No. 1-2, p. 279.

[17] Y.N. Wang, Y.P. Bao, M. Wang, and L.C. Zhang, Precipitation and control of BN inclusions in 42CrMo steel and their effect on machinability, *Int. J. Miner. Metall. Mater.*, 20(2013), No. 9, p. 842.

[18] K. Yamada, M. Igarashi, S. Muneki, and F. Abe, Creep properties affected by morphology of MX in high-Cr ferritic steels, *ISIJ. Int.*, 41(2001), p. s116.

[19] L.K. Singhal and J.W. Martin, The nucleation and growth of widmannstätten $M_{23}C_6$ precipitation in an austenitic stainless steel, *Acta Metall.*, 16(1968), p. 1159.

[20] C. Zener, Theory of growth of spherical precipitates from solid solution, *J. Appl. Phys.*, 20(1949), p. 950.

[21] L.Q. Xu, D.T. Zhang, Y.C. Liu, B.Q. Ning, Z.X. Qiao, Z.S. Yan, and H.J. Li, Precipitation kinetics of $M_{23}C_6$ in T/P92 heat-resistant steel by applying soft-impingement correction, *J. Mater. Res.*, 28(2013), No. 11, p. 1529.

[22] E.A. Brandes, *Smithells Metals Reference Book*, Butterworths, London, 1983, p. 13.

[23] J. Guo, H.W. Qu, L.G. Liu, Y.L. Sun, Y. Zhang, and Q.X. Yang, Study on stable and meta-stable carbides in a high speed steel for rollers during tempering processes, *Int. J. Miner. Metall. Mater.*, 20(2013), No. 2, p. 146.

[24] K. Sawada, M. Taneike, K. Kimura, and F. Abe, *In situ* observation of recovery of lath structure in 9% chromium creep resistant steel, *Mater. Sci. Technol.*, 19(2003), p. 739.

[25] F. Abe, Coarsening behavior of lath and its effect on creep rates in tempered martensitic 9Cr–W steels, *Mater. Sci. Eng. A*, 387-389(2004), p. 565.

[26] G. Krauss, Martensite in steel: strength and structure, *Mater. Sci. Eng. A*, 273-275(1999), p. 40.